Baseline-Free Impact Localization in Plate Structures Using a Combined SA-GA Optimization Framework

Hussain Altammar, Mohammad Faseeulla Khan, Syed Quadir Moinuddin and Saad Arif

Department of Mechanical Engineering, College of Engineering, King Faisal University, Al-Ahsa 31982, Saudi Arabia. E-mail: haltammar@kfu.edu.sa

Fatih Selimefendigil

Department of Mechanical Engineering, Manisa Celal Bayar University, 45140 Manisa, Turkey.

(Received 20 September 2025; accepted 27 February 2026)

Accurate impact localization remains challenging for structural health monitoring (SHM) systems due to wave propagation complexities and high measurement uncertainties. This study presents a novel baseline-free framework that combines simulated annealing (SA) and genetic algorithm (GA) to characterize low-velocity impacts in plate structures. The proposed framework provides robust impact localization without relying on baseline signals, material properties, or detailed geometric parameters. Experimental impact tests were conducted using a coarse network of piezoelectric sensors arranged in multiple configurations to evaluate the performance of the proposed framework for impact characterization, full-field group velocity mapping, and computational efficiency. The framework predicted impact locations with an average relative error of less than 5% and R-values of about 0.98 under the optimal sensor configuration. The analysis of sensor placement indicated asymmetric sensor layouts yield 50% higher performance compared to symmetric layouts. The combined SA-GA framework successfully identified various impacts both inside and outside the regions confined by active sensor network with probabilities exceeding 90%. Additionally, the results demonstrated that the proposed framework consistently outperformed standalone SA and GA algorithms in both impact identification accuracy and the consistency of the velocity field.

1. INTRODUCTION

Global optimization algorithms such as Genetic Algorithm (GA), Particle Swarm Optimization (PSO), and Simulated Annealing (SA) have been widely applied in SHM for impact localization, damage detection and sensor placement due to their ability to handle noisy measurements and nonlinear inverse problems.[1–3] These standalone methods have demonstrated effectiveness in estimating impact coordinates, wave velocities, and structural parameters, particularly in plate-like structures where dispersion and multimodal wave propagation complicate deterministic solutions.[4,5] However, many existing optimization-based SHM frameworks rely on baseline signals, material properties, or detailed geometric models, which limits their applicability in practical scenarios where such information is unavailable or uncertain. In contrast, the combined SA and GA approach proposed in this work is formulated for the ill-posed and baseline-free inverse problem of impact localization. The framework is designed to address solution multiplicity and measurement uncertainty without requiring prior baseline data as well as material and geometric parameters.

Beyond stand-alone global optimization methods such as GA, PSO, and SA, recent research has emphasized hybrid frameworks that combine global exploration with local refinement to address the challenges of multimodal and non-convex search spaces.[6–9] Memetic algorithms have emerged as a powerful paradigm by embedding local search mechanisms within evolutionary algorithms, thereby improving convergence reliability and solution quality.[10,11] Hybrid evolutionary-local search schemes have demonstrated superior performance in large-scale combinatorial optimization and inverse problems, particularly when solution landscapes exhibit strong multimodality.[8] Practical guidelines for designing such hybrid frameworks highlight the importance of balancing exploration and exploitation to avoid premature convergence while maintaining computational efficiency.[9] Additional studies in engineering optimization have shown that hybrid metaheuristics incorporating local refinement outperform classical evolutionary algorithms in structural design, scheduling, and parameter identification tasks.[12] Broader analyses of metaheuristic design principles further emphasize that hybridization is often essential for robust performance in real-world optimization problems characterized by uncertainty and noise.[13] Recent developments in hybrid PSO-local search and differential evolution local search frameworks also demonstrate improved accuracy in inverse parameter estimation and damage detection, reinforcing the value of combining global and local search operators in SHM-related applications.[14–18] These studies collectively underscore the relevance of hybrid optimization strategies, where the trade-off between computational cost and solution accuracy must be carefully managed in practical engineering settings.

The reliable detection of impact events has emerged as a critical capability for modern SHM systems to address the growing need to identify barely visible impact damage (BVID) that often precedes failures in aerospace, civil, and energy structures.[19–21] This proactive monitoring approach represents a paradigm shift in asset management, enabling real-time structural condition assessment that improves safety while reducing life-cycle costs.[22,23] Impact monitoring systems leverage advance sensing technologies such as piezoelectric wafer active

sensors (PWAS), fiber Bragg grating (FBG) arrays, and strain gauges.[24,25] This technological diversity reflects the complex trade-space between sensitivity, coverage density, and installation constraints across different engineering applications. This study presents an optimization framework combining SA and GA to yield low-velocity impact characteristics and group velocity mapping of A0 mode in plate structures integrated with piezoelectric sensors.

Time-difference-of-arrival (TDoA) methodology has gained prominence as an effective geometric approach for impact monitoring. Its application has been successfully demonstrated across various engineered systems including aerospace-grade composites, advanced polymer structures, and additive-manufactured components.[26–28] The complex nature of impact-induced elastic waves presents significant characterization challenges due to their inherent dispersion and multimodal propagation characteristics.[29,30] These phenomena introduce substantial uncertainty in time-of-flight determination from sensor signals, complicating accurate impact localization. Recent advances in uncertainty quantification have led to the development of advance analytical frameworks to address these limitations, including probabilistic methods, Bayesian inference techniques, fuzzy logic systems.[31–36] These approaches have demonstrated improvements in impact identification reliability, simultaneously enhancing localization precision while reducing false positive rates in SHM applications. The integration of such advanced computational techniques represents a paradigm shift in SHM capabilities, enabling more robust assessment of both impact events and damage conditions.

Recent developments in SHM have demonstrated the significant potential of optimization-driven signal processing techniques for improving impact detection and localization accuracy. Global optimization algorithms including GA, PSO, and SA have shown particular effectiveness in solving complex and multi-objective problems.[37–39] Research indicates that supplementing traditional TDoA methods with these optimization approaches yields substantially improved results. The adaptability of these methods is evident in advanced material systems, where optimization methods have successfully addressed wave propagation complexities in laminated composites.

These methods have also proven effective for error reduction in acoustic emission analysis for composite materials and optimization of sensor arrays to maximize system sensitivity and monitoring coverage.[40,41] They have shown to be promising to address wave speed prediction in anisotropic materials, optimal sensor grid configuration, and impact localization in complex structures through optimized sensor placement.[42,43]

Sensor measurement uncertainties are particularly problematic for impact localization, where aging infrastructure and environmental changes significantly influence measurement reliability.[44,45] Measurement quality directly affects localization accuracy. Although increasing sensor density reduces uncertainty, it increases computational costs. Machine learning approaches offer promising alternatives for handling these multi-dimensional problems, but require extensive training datasets to establish robust input-output relationships.[46–48]

This paper presents an optimization framework integrating SA and GA to achieve accurate low-velocity impact localization and group velocity mapping in plate structures while effectively minimizing uncertainties. The framework formulation, including group velocity mapping, is described first, followed by details of the experimental setup for impact testing. The subsequent section discusses validation analysis through wave mode characterization using dispersion curves. A comparative evaluation of the optimization algorithms performance and efficiency across different impact points and sensor configurations was considered next. The study concludes by summarizing key findings and observations.

2. MATERIALS AND METHODS

2.1. Impact Characterization

A low-energy impact on a thin plate induces localized elastic deformation at the contact point as kinetic energy transfers to the structure. This deformation generates radially propagating elastic waves, predominantly in the form of fundamental Lamb wave modes. These low-frequency wave components exhibit propagation velocities governed by the plate material properties and thickness characteristics. Accurate determination of impact coordinates (x, y) and wave propagation velocity C requires a minimum of four strategically positioned sensors to capture time delays of acoustic wavefronts. As illustrated in Fig. 1, piezoelectric sensors are arranged in a spatial distribution, with four transducers positioned at each corner S_1 at (x_1, y_1), S_2 at (x_1, y_2), S_3 at (x_3, y_3), S_4 at (x_4, y_4), and the fifth sensor S_5 located at the center (x_5, y_5) of the plate, establishing a two-dimensional coordinate reference system for impact localization. The experimental configuration incorporates a fifth sensor S_5 to enable comparative analysis of different array geometries and their influence on localization accuracy.

For a thin a piezoelectric sensor operating in d_{31}, the sensing direction is along the poling axis (3-direction). The constitutive equation can be simplified as:[49]

$$D_3 = d_{31} T_1 + \varepsilon_{33}^{\mathrm{T}} E_3. \tag{1}$$

The direct piezoelectric effect mathematically represented in Eq. (1) shows how mechanical stress T_1 along the 1-axis induces electric displacement D_3 along the orthogonal 3-axis. In open-circuit sensing mode, the total charge generated by impact-induced strain waves on the electrodes is obtained by:

$$Q = \int_A D_3 \, dA = d_{31} \int_A T_1 \, dA. \tag{2}$$

The voltage across a piezoeelctric sensor connected to a high-impedance is defined as:

$$V = \frac{d_{31} F h}{2 \varepsilon_{33}^{\mathrm{T}} A}; \tag{3}$$

where F is the impact force, A is the electrode area, and h is the thickness of the piezoelectric sensor.

Upon elastic waves reaching piezoelectric sensors, the propagating elastic waves induce time-varying strain fields that are transduced into corresponding voltage signals. These acquired waveforms encode essential characteristics for impact analysis such as arrival times, amplitude variations, and spectral content. The TDoA technique leverages these temporal features across multiple sensor locations to geometrically triangulate the impact source position.[50] The wave propagation paths from impact location to each sensor are denoted as d_1 through d_4. These path length differences correlate directly with measured time delays Δt_{i1} through the group velocity relationship.

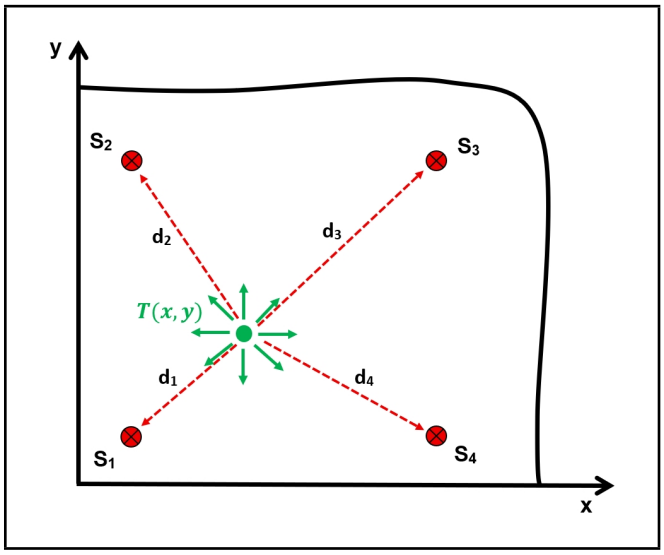

Figure 1. Plate diagram of a network of piezoelectric sensors and impact located at $T(x, y)$.

While mathematical formulations presented here consider four-sensor configurations, the experimental configuration incorporates a fifth sensor S_5 to enable a comparative analysis of different array geometries achieved by activating different combinations of four sensors to study their influence on localization accuracy. The propagation distance from the impact to the i-th sensor is denoted as d_1, while d_1 specifically represents the path length to the reference sensor S_1. The time delay Δt_{i1} quantifies the difference in wavefront arrival duration between the reference sensor S_1 and the i-th sensor.

Wavefront detection is implemented through a threshold-crossing method applied to the measured signals $V_i(t)$. The arrival time t_i for each sensor is mathematically defined as the first instance where the voltage signal exceeds a predetermined threshold. To compute the time delays Δt_{i1}, the time of arival (ToA) of S_1 is set as a reference derive the system of equations as:

$$d_{i-1} - d_1 - C\Delta t_{i1} = 0, \quad i = 2, 3, 4. \tag{4}$$

Using the Euclidean distance formula, the distances d_i are computed in terms of impact location (x, y) and sensor coordinates (x_i, y_i). Substituting the geometric relationships into the system of equations yields:[5]

$$f_{i-1} = \sqrt{(x_i - x)^2 + (y_i - y)^2} - \sqrt{(x_1 - x)^2 + (y_1 - y)^2} - C\Delta t_{i1} = 0, \qquad i = 2, 3, 4. \tag{5}$$

The impact location can be solved deterministically by finding the common intersection point of these hyperbolic curves, representing the spatial solution that simultaneously satisfies all time-delay measurements. For the sake of comparison with deterministic methods, measured propagation time delays between sensor pairs are used to construct hyperbolic curves whose intersection defines the probable impact coordinates.

2.2. Optimization Framework

2.2.1. Optimization Problem Formulation

The inherent nonlinearity of the hyperbolic equation system presents significant computational challenges, including solution multiplicity, trivial solutions, and a potential non-existence solution. To overcome these limitations, an optimization-based approach utilizing SA and GA was developed with group velocity incorporated as an optimization design parameter. The selection of SA and GA was based on their complementary strengths for solving the nonlinear, multimodal inverse problem of impact localization. GA is excellent for broad, population-based exploration of the solution space, while SA provides a probabilistic mechanism for fine-tuning and escaping local optima. Their combination is specifically designed to address the challenges of solution multiplicity and measurement uncertainty inherent in baseline-free localization.

The optimization process systematically minimizes both solution error and associated uncertainties. The problem is formulated through an objective function $Z(\mathbf{X})$ that quantifies the residual errors between predicted and observed wave propagation characteristics:[5]

$$Z(\mathbf{X}) = \sum_{i=2}^{4} \left[\left(\sqrt{(x_i - x)^2 + (y_i - y)^2} - \sqrt{(x_1 - x)^2 + (y_1 - y)^2} - C\Delta t_{i1} \right)^2 \right]. \tag{6}$$

The optimization problem is solved under physically admissible bounds to ensure meaningful and stable solutions. The design vector is defined as $\mathbf{X} = [x,\, y,\, C]^T$, where (x_i, y_i) denotes the coordinates of the i-th sensor, and (x, y) represents the unknown impact location. All design variables are restricted to positive values, reflecting the physical nature of the coordinate system and the group velocity. No geometric constraints or shape-dependent assumptions are imposed on the domain, which allows the formulation to operate independently of plate geometry. Consequently, the method remains applicable to structures of arbitrary size, aspect ratio, or boundary configuration.

2.2.2. SA and GA

The nonlinear inverse problem was addressed using a two-stage optimization framework combining SA and GA. These methods were selected for their complementary strengths in global search capability and local minima avoidance. The SA stage begins with an initial estimate $\mathbf{X}_0$ and an initial temperature $T_0 = 100$ K. A multiplicative cooling schedule is adopted, in which the temperature at iteration q is updated according to:[12]

$$T_q = \gamma\, T_{q-1}; \tag{7}$$

with a cooling factor $\gamma = 0.95$. This gradual reduction in temperature governs the transition from exploratory behavior at high temperatures to more conservative, exploitation-focused behavior as the temperature decreases. At each temperature level, a trial solution $\mathbf{X}_{\text{new}}$ is generated by perturbing the current state $\mathbf{X}_k$ within bounded limits.

The decision to accept or reject the trial point is based on a probabilistic rule that favors improvements but still allows occasional uphill moves. If the objective function decreases, the new point is accepted outright. Otherwise, acceptance occurs with a probability that depends on the increase in objective value and the current temperature:

$$\mathcal{M}_{\text{accept}} = \frac{1}{1 + \exp\left(\dfrac{Z(\mathbf{X}_{\text{new}}) - Z(\mathbf{X}_k)}{T_k} \right)}. \tag{8}$$

Because both the objective difference and the temperature are positive for uphill moves, this probability lies strictly between 0 and $\frac{1}{2}$. As the temperature decreases, the likelihood of accepting inferior solutions diminishes, thereby reducing random wandering and encouraging convergence toward a stable solution. The SA phase continues until the temperature falls below a prescribed minimum value or until no further improvement is observed over a fixed number of iterations. The best solution obtained from this stage is then combined with the GA.

The GA was then implemented to solve the non-linear optimization problem. The algorithm follows a population-based approach, leveraging selection, crossover, and mutation operators to explore the solution space. The algorithm was initialized with a population size of n and candidate solutions $\mathbf{P}_k = \{\mathbf{X}_1, \mathbf{X}_2, \ldots, \mathbf{X}_n\}$, where each $\mathbf{X}_i$ represents a potential solution of a real-valued vector. The population size was set to 50, and the maximum number of generations was defined as 100 times the number of design variables, allowing sufficient evolution.

Each solution $\mathbf{X}_i$ in the population was evaluated using an objective function $Z(\mathbf{X}_i)$. To align with GA conventions, the objective function was transformed into a fitness value $F(\mathbf{X}_i)$, where higher fitness corresponded to better solutions. For minimization problems, the transformation was:

$$F(\mathbf{X}_i) = -Z(\mathbf{X}_i). \tag{9}$$

Parents are selected via stochastic uniform sampling, favoring individuals with higher probability of selection. The probability p_i of selecting a solution $\mathbf{X}_i$ is given by:[12]

$$p_i = \frac{F(\mathbf{X}_i)}{\sum_{j=1}^{n} F(\mathbf{X}_j)}. \tag{10}$$

For two parents $\mathbf{X}_a$ and $\mathbf{X}_b$, offspring were generated by intermediate crossover:

$$\mathbf{X}_{\text{child}} = \mathbf{X}_a + \theta(\mathbf{X}_b - \mathbf{X}_a); \tag{11}$$

where θ is a random weighting factor. To preserve the best solutions across generations, the top elites of the population are carried forward unaltered. The algorithm iterated until either, a maximum number of generations $G_{\max}$ was reached, or the population converged below a threshold ϵ. In this study, crossover fraction of 0.8 was assigned to regulate the proportion of offspring produced through crossover, while elite count was determined as 5% times the population size to retain the fittest individuals.

To evaluate the performance of the proposed framework, the relative error between the predicted and the actual values is determined. Additionally, the correlation coefficient (R^2) in the x and y coordinates for different impact locations were also computed as:

$$R_x^2 = 1 - \frac{\sum_{k=1}^{n}\sum_{i=1}^{n}(x_{k,i} - \hat{x}_{k,i})^2}{\sum_{k=1}^{n}\sum_{i=1}^{n}(x_{k,i} - \bar{x})^2}; \tag{12}$$

$$R_y^2 = 1 - \frac{\sum_{k=1}^{n}\sum_{i=1}^{n}(y_{k,i} - \hat{y}_{k,i})^2}{\sum_{k=1}^{n}\sum_{i=1}^{n}(y_{k,i} - \bar{y})^2}; \tag{13}$$

where $x_{k,i}$ and $y_{k,i}$ are actual observed values, $\hat{x}_{k,i}$ and $\hat{y}_{k,i}$ are the predicted values from linear fit model, and $\bar{x}$ and $\bar{y}$ are the grand mean of actual values.

The velocity mapping approach combines SA and GA optimization with spatial interpolation techniques. The method begins by determining group velocity values at discrete grid points across the structure. These discrete velocity estimates are then interpolated to generate a full-field velocity map. The probability distribution of group velocity values is established through statistical analysis of $N = 100$ optimization iterations. For each grid point, the probability associated with the j-th velocity interval $\mathcal{V}_j$ is computed as:

$$p(C \in \mathcal{V}_j) = \frac{1}{N}\sum_{q=1}^{N}\mathbb{I}\big(C_q \in [C_j^{\min}, C_j^{\max})\big); \tag{14}$$

where $\mathbb{I}(\cdot)$ is the indicator function. The most probable group velocity at a test location is taken as the midpoint of the interval with the highest probability:

$$C_n^* = \frac{C_{j^*}^{\min} + C_{j^*}^{\max}}{2}, \qquad j^* = \arg\max_j p(C \in \mathcal{V}_j). \tag{15}$$

After the optimal velocities C_{mn}^* are obtained at the grid points (x_m, y_n), a continuous velocity field is generated using standard bilinear interpolation. In this step, the velocity at any location within a grid cell is computed by weighting the four surrounding nodal values according to the relative position of the point inside the cell. The interpolation weights depend on the normalized distances in the x- and y-directions, ensuring a smooth transition between adjacent grid points. In parallel with velocity estimation, the framework also constructs probability mass functions for the predicted impact coordinates. For each spatial interval $\bar{X}_k$ and $\bar{Y}_l$, the probabilities are computed as:

$$p(x \in \bar{X}_k) = \frac{1}{N}\sum_{q=1}^{N}\mathbb{I}\big(x_q \in [x_k^{\min}, x_k^{\max})\big); \tag{16}$$

$$p(y \in \bar{Y}_l) = \frac{1}{N}\sum_{q=1}^{N}\mathbb{I}\big(y_q \in [y_l^{\min}, y_l^{\max})\big); \tag{17}$$

where $\bar{X}_k$ and $\bar{Y}_l$ denote the coordinate bins for the x- and y-directions. These distributions provide a probabilistic representation of the predicted impact location.

2.3. Experiments

2.3.1. Experimental Setup

The impact testing apparatus, shown in Fig. 2(a), features a $300 \times 300 \times 0.61$ mm^3 aluminum plate mounted within a drop-test mechanism. This system enables controlled impact testing through a guided steel ball (5mm diameter, mass $m = 0.513$ g) released from a predefined height of 540 mm. The impact energy delivered to the plate, accounting for the elastic rebound characteristics of the steel-aluminum contact, is estimated to be approximately 1.15 mJ. This configuration ensures repeatable low-velocity impact condition across all experimental trials. The material properties of sensors, aluminum plate and the steel ball are provided in Table 1. The drop test mechanism incorporates two-axis positioning capability: a sliding tube adjusts x-coordinate impacts along its slot, while the sample carrier provides y-coordinate positioning, allowing impacts

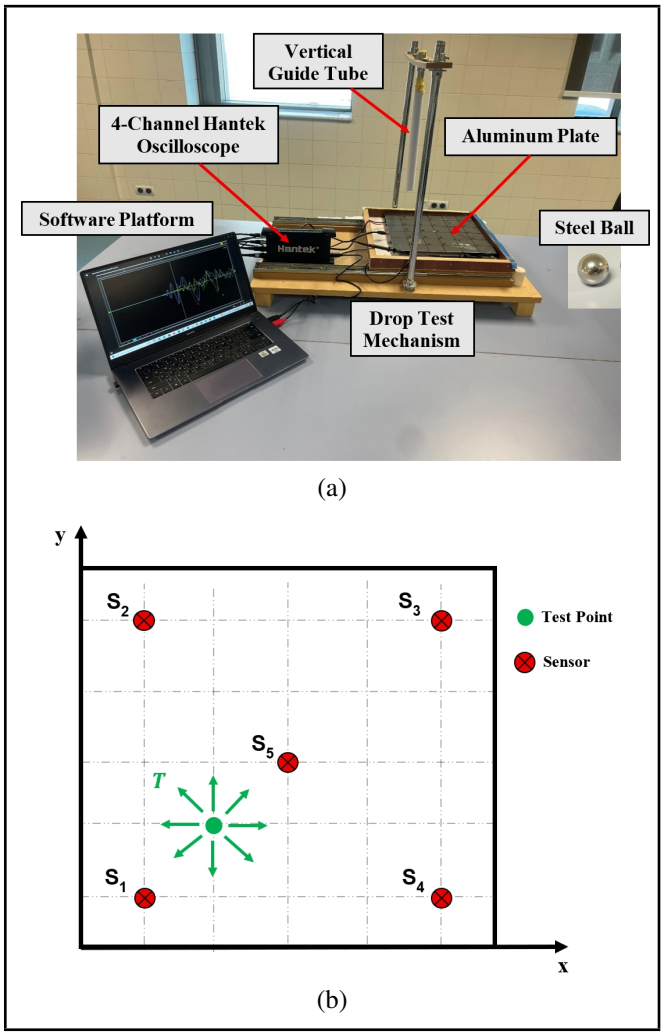

Figure 2. (a) Experimental setup, (b) schematic of the aluminum plate showing the 25 predefined impact test points in a 50 mm grid. The positioning uncertainty of impact events is estimated at ±5 mm.

Table 1. Material properties of PZT, aluminum, and steel used in experiments.

Properties	Symbol	PZT	Aluminum	Steel
Piezoelectric coefficient (10^{-12} C/N)	d_{31}	-276	—	—
	d_{33}	630	—	—
Electromechanical coupling factor (%)	k_{31}	0.40	—	—
Density (kg/m^3)	ρ	7800	2700	7830
Young's modulus (10^9 N/m^2)	E	0.5	68.9	207.0
Poisson's ratio	ν	0.31	0.33	0.30

at any of 25 predefined grid points (Fig. 2(b)) for comprehensive velocity field mapping. The 50 mm grid spacing provides a balance between spatial resolution for full-field velocity mapping and experimental repeatability. The nominal positioning uncertainty is ±5 mm. The framework prediction accuracy is evaluated against these nominal target locations.

The aluminum plate rests on vibration-isolating foam supports to minimize external interference with wave propagation measurements. Five piezoelectric sensors (11 mm diameter, 0.4 mm thickness) are bonded to the bottom surface of the plate using non-conductive adhesive. A four-channel Hantek oscilloscope records the sensor outputs at 1.25 MHz sampling rate, capturing 4096-sample waveforms per impact. Edge triggering synchronizes data acquisition across all channels when signals exceed a predefined voltage threshold, ensuring precise temporal alignment of impact events. All acquired waveforms are digitally stored for subsequent processing and analysis.

Table 2. Configurations of active piezoelectric sensors and their respective coordinates.

	S_1	S_2	S_3	S_4	S_5
S1234 Config.	✓	✓	✓	✓	x
S1235 Config.	✓	✓	✓	x	✓
S1245 Config.	✓	✓	x	✓	✓
x (mm)	50	50	250	250	150
y (mm)	50	250	250	50	150

The experimental configuration incorporates five piezoelectric sensors arranged in a square pattern with a central element. This layout maintains minimum 50 mm clearance from plate edges and 200 mm inter-sensor spacing to minimize boundary reflections and ensure clear wavefront detection. Four sensors are actively monitored during each test, enabling evaluation of three distinct array arrangements. The network configurations along with global coordinates of piezoelectric sensors are provided in Table 2. The sensor coordinates listed in Table 2 are fixed inputs to the optimization framework, representing predefined geometric arrangements under evaluation. They are not variables optimized by the SA-GA algorithm, which solves only for the impact location and group velocity. The three specific sensor configurations were selected to systematically evaluate the performance of asymmetric versus symmetric arrays. This design allows us to investigate how geometry influences spatial resolution and localization accuracy for impacts both inside and outside the sensor regions, which is critical for practical SHM network design.

The acquired voltage signals undergo pre-processing using a Savitzky-Golay filter.[51] This filter is a computationally efficient smoothing technique that maintains critical waveform features while reducing noise. A first-degree polynomial with a 43-window was employed in this study for its advantages of computational efficiency and signal integrity preservation. The conditioned time-domain signals are subsequently analyzed in the frequency domain through application of the Fast Fourier Transform (FFT). The frequency-domain representation of the smoothed voltage signal $\hat{V}(j)$ is obtained by evaluating its discrete Fourier transform. For the k-th spectral component, the transform can be written as:

$$H(k) = \sum_{j=0}^{n-1} \hat{V}(j)\, \exp\left(-i\, 2\pi\, \frac{k\, j}{n}\right). \tag{18}$$

Here, $H(k)$ denotes the complex amplitude associated with the k-th frequency bin, n is the total number of uniformly sampled time points, and j indexes the samples in the time domain. The exponential factor $\exp(-i\, 2\pi kj/n)$ serves as the oscillatory kernel that projects the time-domain signal onto its harmonic components.

The signal-to-noise ratio (SNR) serves as a key metric for evaluating the quality of impact-induced waveforms. Thus, the root mean square (RMS) of waveform signals is computed as follows:

$$V_{\text{RMS}} = \sqrt{\frac{1}{\tau}\int_0^{\tau} V(t)^2 dt}; \tag{19}$$

where τ denotes the measurement time period. The G_{SNR} in decibels (dB) is then derived as:

$$G_{\text{SNR}} = 20\log_{10}\left(\frac{V_{\text{RMS}}}{V_{\text{noise}}}\right); \tag{20}$$

with V_{noise} corresponding to the RMS noise amplitude. For reliable impact detection, the SNR should be maintained be-

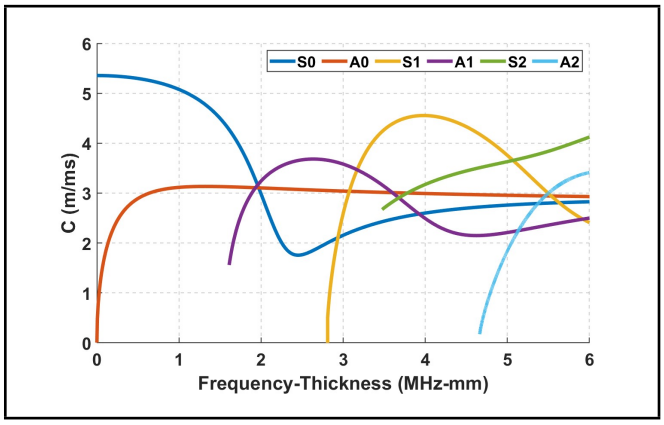

Figure 3. Dispersion curves of fundamental Lamb modes in a 0.61 mm thick aluminum plate.

tween 10−15 dB to ensure adequate signal distinction from background noise.

3. RESULTS AND DISCUSSION

3.1. Waveform Analysis

3.1.1. Signal Characteristics

Analysis of Fig. 3 reveals the distinct velocity characteristics of fundamental modes: the symmetric (S0) wave propagates much faster than the antisymmetric (A0) wave at low excitation frequencies, suggesting separable arrivals in recorded waveforms. The waveform signals and time delays for test point, T4 are provided in Fig. 4(a). The recorded signals exhibit consistent temporal features, with initial wavefronts corresponding to direct impact waves followed by successive boundary reflections. This characteristic propagation pattern is systematically observed in all sensor measurements, confirming proper wave transmission through the plate structure. Signal quality assessment revealed a minimum signal-to-noise ratio of 11 dB across all channels. This favorable SNR enabled reliable time-of-arrival detection through a fixed 0.5 V threshold, which was uniformly applied to all sensors. The signals from sensors show that the elastic waves arrive S_4 sensor first with a negative time delay of 195 µs relative signal received by S_1, while positive delay recorded for the other signals suggesting that these signals lag the reference signal. These signals exhibit high amplitude peaks, which is attributed to reflection from the plate boundaries. The signals show matching trends but different timing for reflection.

The frequency spectra of waveform signals are provided in Fig. 4(b) along with the group velocity dispersion curve of A0 mode for the 0.61 mm thick aluminum plate. The dispersion curve of A0 indicates the exclusive excitation of the A0 Lamb mode in the plate. Generally, transverse impact conditions mostly excite the A0 mode, which consequently carries the dominant portion of the impact energy, while the S0 mode contribution remains negligible under such loading conditions. This modal selectivity arises from the low amplitude of the S0 mode, which falls below the detectable threshold of the acquisition system given the inherent noise floor of voltage measurements. The dominant frequency of received waveform signals in Fig. 4(b) is ranging between 500 and 2000 Hz. Higher frequency A0 waves are expected to travel faster, and consequently arrive sooner to sensors. Thus, the first arrival A0 waves are anticipated to have a group velocity of about 500 m/s

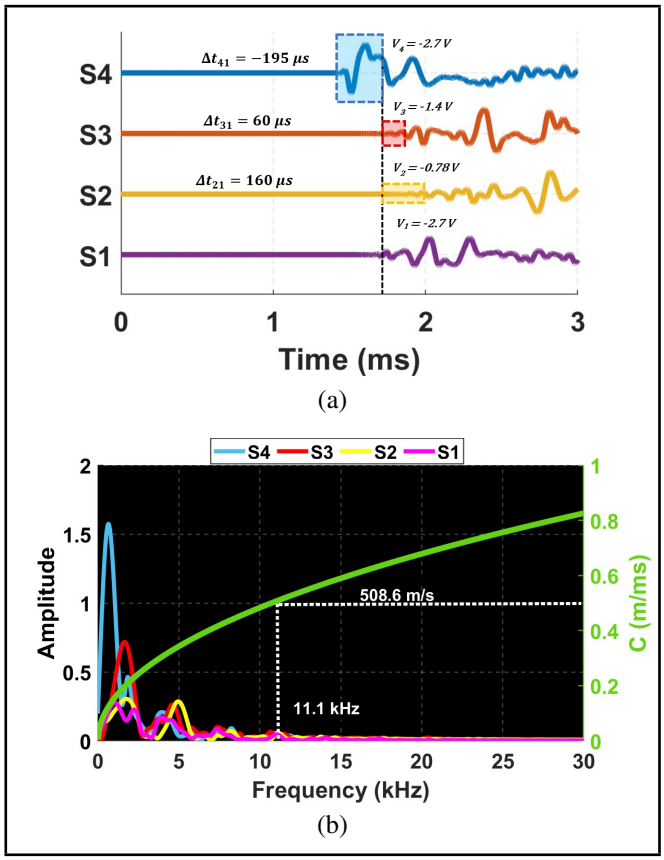

Figure 4. (a) Voltage waveforms obtained for impact at T4 under square sensor configuration, (b) frequency spectra and dispersion curve of A0 mode for 0.61 mm thick aluminum plate.

at 11.1 kHz as labeled in Fig. 4(b). This frequency observed across all received waveform signals which further reinforces the observation of wave propagation in a homogeneous plate.

3.2. Impact Localization

3.2.1. Comparison Analysis of Optimization Algorithms

Figure 5 compares the performance of optimization algorithms, SA, GA, and the combined SA-GA, for impact T3 which occurred at $x = 150$ mm, $y = 50$ mm. The figure presents PMFs for impact coordinates and group velocity, providing insights into the accuracy and reliability of each method. In Fig. 5(a)-(c), the standalone SA method shows moderate precision in x-coordinate determination but exhibits substantial dispersion in y-coordinate predictions, suggesting limitations in vertical localization capability. Similarly, GA displays comparable challenges with y-coordinate estimation despite adequate x-coordinate performance, indicating this may be a fundamental limitation of individual optimization approaches. The SA-GA framework, by contrast, achieves remarkably sharp PMF peaks for both coordinates at the actual impact. This performance indicates the combined SA-GA approach can potentially overcome the weaknesses of standalone algorithms.

The combined SA-GA approach achieved better results by leveraging the complementary strengths of both methods while mitigating their individual weaknesses. SA excels at fine-tuning solutions through local exploitation but suffers from high variability due to its stochastic nature, often getting trapped in local optima. In contrast, GA performs broader ex-

ploration of the solution space but can prematurely converge to suboptimal solutions. By averaging their independent results, the combined SA-GA effectively compensates for these limitations, SA random deviations and GA occasional biases partially cancel each other out, leading to a more accurate and stable final prediction. This error-compensation effect is particularly valuable in impact localization problems, where small measurement errors in wave velocity or arrival time can lead to significant deviations in predicted coordinates.

The group velocity estimation results in Fig. 5(d)-(f) follow a parallel pattern. The standalone SA and GA produce widely dispersed velocity PMFs that reflect considerable uncertainty in wave speed determination. The combined SA-GA framework again demonstrates superior performance, generating a narrow, well-defined peak at the expected wave speed that indicates both higher accuracy and lower uncertainty in velocity estimation. The subsequent analyses further examine the combined SA-GA for impact localization and group velocity determination.

3.2.2. Effect of Sensor Arrangement

The impact test points considered in this analysis are inside and outside the region confined by active sensors. The performance characteristics of the combined SA-GA framework are provided in Table 3 and Fig. 6. Table 3 summarizes the SA-GA outputs of PMFs and relative errors for different test points under three sensor arrangements. The results exhibit clear dependence on sensor placement with significant variations in localization accuracy across different arrangements. For test point T4 illustrated in Fig. 6(a)-(c), the S1245 configuration demonstrates perfect x-coordinate prediction probability (100%) with low uncertainty (± 4 mm) and error (2%), while the S1234 arrangement shows substantially wider dispersion (± 15 mm) at 63% probability. This pattern continues for y-coordinates at T4, where the results obtained from S1245 arrangement maintain 99% probability with ± 3 mm uncertainty compared to 75% probability at ± 25 mm uncertainty under square arrangement.

Similar improvements emerge when examining T11 results in Fig. 6(d)-(f). The triangular configurations achieve 98% x-coordinate prediction probabilities with tight uncertainty bounds (± 4 to ± 6 mm) and lower relative errors of less than 6%, while the square arrangement in Fig. 6(d) shows broader distributions (± 26 mm) and higher relative error. By contrast, the y-coordinate prediction for T11 under S1245 configuration reaches 100% probability with high precision (± 2 mm) and accuracy (1.6%).

The framework capability to handle diverse impact locations becomes evident when analyzing T21 results in Fig. 6(g)-(i). While all configurations show some performance degradation for this test point, the triangular arrangements still maintain superior probabilities (73–86% for x, 79–94% for y) compared to the square configuration. It can be noted that the y-coordinate prediction at T21 under S1235 arrangement predicted 94% probability with ± 13 mm uncertainty and 3.3% relative error.

The correlation analysis in each sub-figure of Fig. 7 represents plotting predicted versus actual values for 25 impact test points in x and y coordinates. The square sensor arrangement in Fig. 7(a)-(b) shows strong linear correlations, with R-values of 0.92 for the x-coordinate and 0.95 for the y-coordinate. The S1235 configuration in Fig. 7(c)-(d) demonstrates noticeable improvements in x-coordinate accuracy as the fitted line more aligns along the diagonal line. Notably, the S1245 arrangement in Fig. 7(e)-(f) achieves the highest performance, with R-values reaching 0.98, suggesting that its sensor geometry optimally balances sensitivity in both directions. The superior performance of asymmetric triangular configurations can be attributed to fundamental geometric advantages in TDoA-based localization. First, these arrangements provide a wider variation in sensor-pair separations and orientations. This diversity increases the crossing angles of the hyperbolic curves defined by Eq. (6) at the impact point, leading to a more distinct and noise-resistant intersection. Second, asymmetric layouts mitigate ambiguity that arises in symmetric configurations when impacts occur near geometric centers or symmetry axes, where similar time delays can make the system of equations ill-conditioned. By breaking spatial symmetry, triangular networks ensure more distinct time delay differences for a wider range of impact locations, thereby improving the conditioning of the optimization problem.

Table 3. Outputs of SA-GA framework for impacts under different sensor arrangements.

Config.	T	P(x)	$\overline{x} \pm \sigma_x$	E_x	P(y)	$\overline{y} \pm \sigma_y$	E_y
S1234	4	63%	204 ± 15	1.3%	75%	76 ± 25	8.6%
S1234	11	63%	68 ± 26	6.0%	59%	137 ± 4	4.3%
S1234	21	67%	64 ± 27	4.6%	63%	206 ± 15	14.6%
S1235	4	88%	184 ± 7	5.3%	73%	79 ± 4	9.6%
S1235	11	98%	67 ± 4	5.6%	90%	140 ± 3	3.3%
S1235	21	73%	44 ± 10	2.0%	94%	240 ± 13	3.3%
S1245	4	100%	206 ± 4	2.0%	99%	76 ± 3	8.6%
S1245	11	98%	67 ± 6	5.6%	100%	145 ± 2	1.6%
S1245	21	86%	37 ± 9	4.3%	79%	235 ± 13	5.0%

These results demonstrate that sensor placement fundamentally affects localization performance. The triangular configurations (S1235 and S1245) consistently outperform the square arrangement (S1234) across all test points, in higher prediction probabilities and lower uncertainty bounds and relative errors. These findings emphasize that while the proposed framework itself is crucial, proper sensor arrangement remains equally vital for achieving high-precision results in SHM applications.

3.3. Group Velocity

3.3.1. Determination of Group Velocity

The SA-GA framework predictions for group velocity under the optimal sensor configuration are summarized in Table 4. It was noticed that edge impacts are associated with higher probability and lower uncertainty in comparison to central impacts. For edge impacts such as T4, the algorithm achieves high probability of 84% for a velocity of 515 m/s with 6.6% uncertainty. This reflects a reliable A0 wave detection. Similarly, the results of T24 maintains good performance (587 ± 36 m/s, 80%). Central impacts, as seen in T13 (150 mm, 150 mm) exhibit higher velocity (599 ± 51 m/s) with 8.5% uncertainty and lower probability (61%). This low probability could be stemmed from symmetric wave propagation patterns that challenge TDoA-based localization. The surface diagram of the objective function shown in Fig. 8 indicates a wide region for the optimal solution, explaining both the expanded velocity range and reduced confidence. Despite that, the proposed optimization framework successfully narrows down the group velocity to a limited range.

3.3.2. Optimization vs. Deterministic Approach

Identical test points from previous analyses are considered herein to enable direct performance comparison. The results

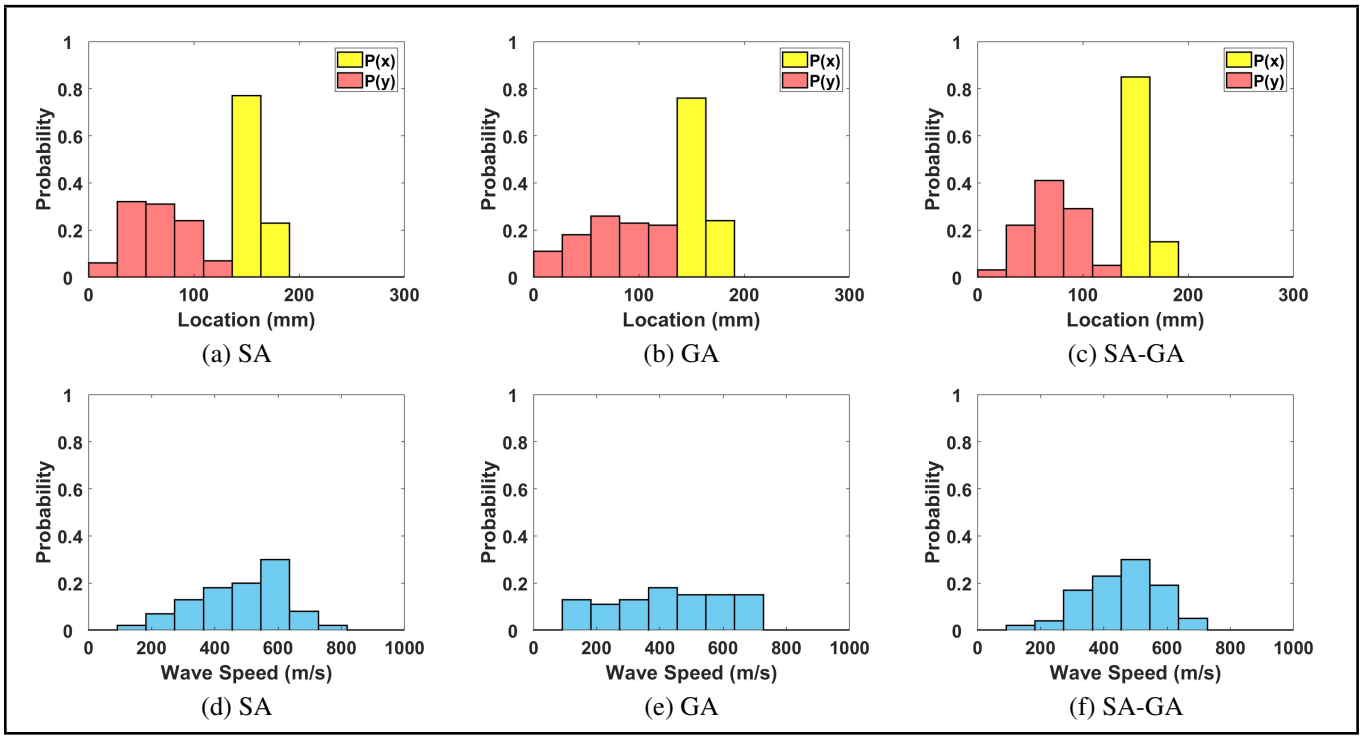

Figure 5. Comparison of optimization algorithm outputs for T3 ($x = 150$ mm, $y = 50$) under S1234 sensor configuration: (a-c) PMFs of impact coordinates; (d-f) PMFs of group velocities.

Table 4. SA-GA optimization algorithm outputs of group velocity under the optimal sensor arrangement.

T	Sensors	Location (mm)		Predicted C (m/s)		
		x	y	Range	$P(C)$	$\overline{C} \pm \sigma_C$
4	1,2,4,5	200	50	454-545	84%	515 ± 34
13	1,2,4,5	150	150	545-636	61%	599 ± 51
21	1,2,4,5	50	250	545-636	70%	561 ± 42
24	1,2,4,5	200	250	545-636	80%	587 ± 36

in Fig. 9 superimposes the hyperbolic functions, the actual impact coordinates, and the SA-GA predicted solution. Hyperbolic curves generated for each sensor pair, using the 11.1 kHz group velocity from dispersion analysis, should theoretically converge at the impact location. However in most cases, it struggles to converge to a single solution evidenced by triple intersections of hyperbolic curves. On the other hand, the proposed optimization framework achieves accurate impact localization, consistently yielding accurate predictions that closely match true impact locations.

Figure 9 demonstrates close agreement between predicted and actual impact locations across all test points, with the combined SA-GA framework showing only minor deviations. The framework performance becomes evident when compared to deterministic methods, which frequently struggle to produce viable solutions even when using the optimal group velocity. Comparative analysis reveals the proposed optimization approach outperformed conventional deterministic methods. The algorithm demonstrates spatial discrimination capability, efficiently isolating high-probability impact zones while excluding regions with low likelihood of impact occurrence. While direct quantitative comparison with literature values (e.g., PSO-based methods) is challenging due to differences in experimental setups, materials, and sensor densities, the achieved sub-5% relative error and probability of detection exceeding 90% without any baseline or material properties represent a significant advancement in reliable, baseline-free impact characterization. By leveraging the combined SA-GA, it provides an accurate and robust impact characteristics without requiring material properties or geometric parameters.

3.3.3. A0 Mode Velocity Mapping

The full-field group velocity distribution over the aluminum plate in Fig. 10 was reconstructed from data collected at 25 physical grid points, with each point tested under three distinct sensor configurations, resulting in a total of 75 processed impact events. These data were analyzed using three optimization methods (SA, GA, and the combined SA-GA) and spatially interpolated using a bilinear technique. Velocities ranged from $450-600$ m/s, with variations attributed to uncertainties in data acquisition, sensor placement, plate geometric and material properties. On the other hand, the two circular low-velocity zones exhibited damping-induced reductions are aligned with the foam supports placed underneath the plate. Overall, the combined SA-GA in Fig. 10(c) produced the most balanced field, mitigating extremes seen in standalone SA and GA results. This spatially resolved velocity mapping enables SHM by tracking localized deviations that could potentially indicate material degradation.

3.4. Computational Efficiency Analysis

The computational performance of SA and GA was evaluated on a standard hardware setup (11^{th} Gen Intel© Core i5, 8 GB RAM) using MATLAB©, with consistent iteration counts (SA: 3500; GA: 50 populations $\times$ 70 generations) to ensure fair comparison. The convergence of SA and GA for a single test point are provided in Fig. 11. For impact test point T4, GA demonstrated high efficiency, requiring 0.0349 s which is about one-third the time of SA (0.1029 s) to reach convergence.

This trend persisted across sensor configurations as shown Table 5, where GA average runtime ranges between $3.1-3.8$ s that is at least 3 times faster than SA, with narrower uncertainty

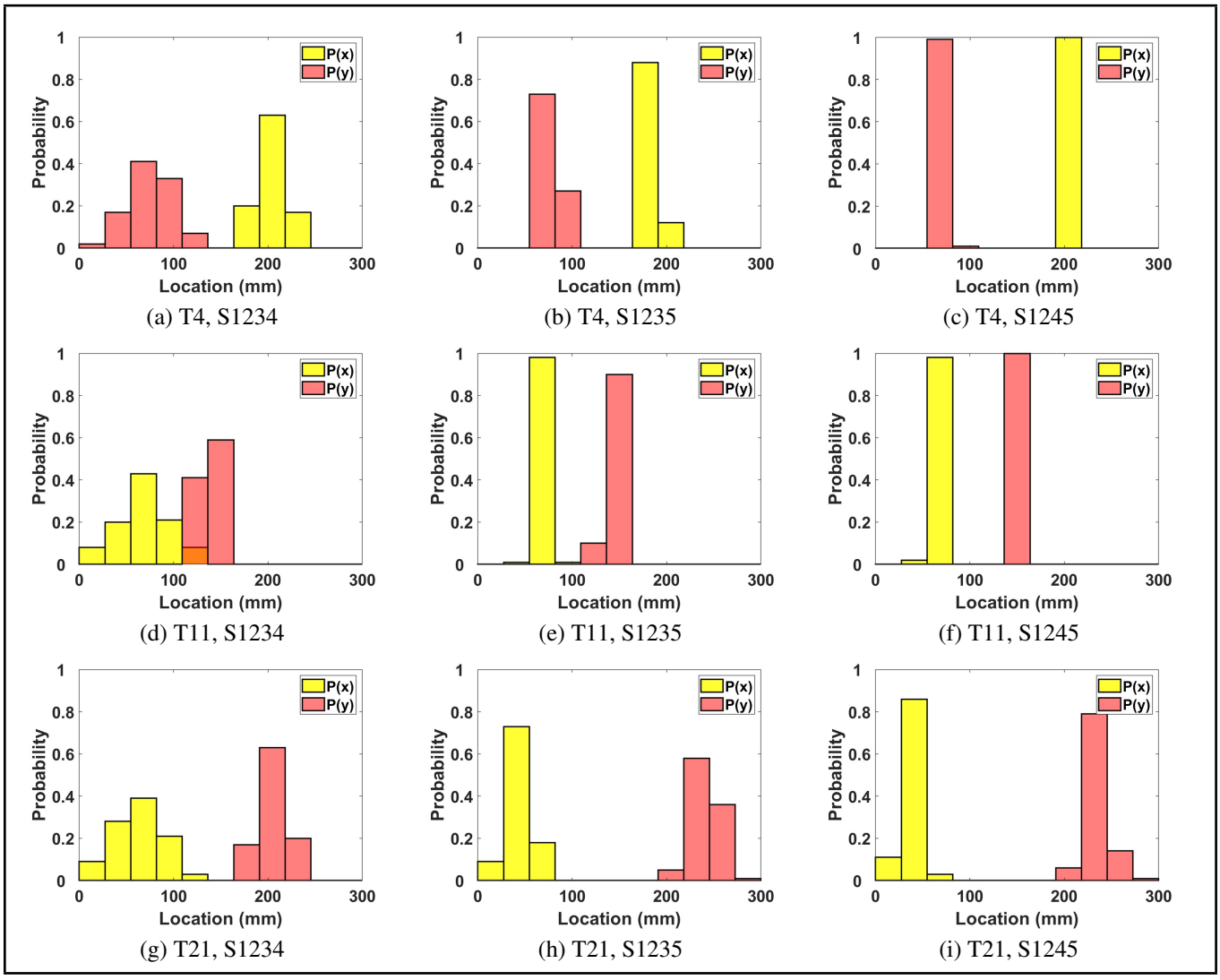

Figure 6. PMFs of impact locations obtained using SA-GA framework under different sensor configurations.

Table 5. Computational time for impact test point, T4.

Sensor configuration	Simulated annealing (s)	Genetic algorithm (s)
S1234	13.1022 ± 0.3954	3.0938 ± 0.0873
S1235	12.5267 ± 0.2616	3.1867 ± 0.0952
S1245	12.2569 ± 0.5260	3.8360 ± 0.1251

bounds. These results represent 100 trials per configuration with 5K data points per test. The disparity stems from fundamental algorithmic differences. GA is a population-based parallel search exploiting concurrent candidate evaluations, while SA utilizes a perturbation-and-acceptance mechanism that incurs iterative overhead. It can be observed from the results that SA runtime decreased with optimized sensor arrangements, whereas GA exhibited an opposite trend. This inverse trend in runtime sensitivity to sensor layouts suggest combined approaches could leverage GA speed for coarse global search and SA precision for local refinement.

While the proposed SA-GA framework consistently demonstrated superior accuracy and robustness compared to standalone GA and SA, it is important to acknowledge the trade-off in computational cost. As illustrated in Fig. 5 and Table 5, standalone GA and SA algorithms can in certain scenarios provide reasonable localization results with lower computational demand. This highlights that engineering judgment should be exercised in practice. When rapid and resource constrained monitoring is prioritized, standalone algorithms may suffice, whereas the SA-GA framework is more suitable for applications requiring higher accuracy under uncertainty. This balance between solution quality and computational efficiency is consistent with broader findings in the literature.[8–10] Thus, the choice of algorithm should be guided by the specific requirements of the SHM application while considering both accuracy and efficiency constraints.

4. CONCLUSIONS AND FUTURE WORK

The experiments conducted herein involve low-velocity impacts on an aluminum plate integrated with a network of piezoelectric sensors. This study has introduced an optimization framework, combining SA and GA for impact characterization in plate structures and group velocity mapping without relying on material properties or baseline signals. Experimental validation across multiple sensor configurations and impact locations demonstrated the framework capability to accurately predict impact characteristics with high probability and low uncertainty. Research key findings include:

- Dispersion curve analysis and experimental validation confirmed the dominant A0 Lamb wave mode as the primary energy carrier with a center frequency of 11.1 kHz.
- The framework achieved impact localization probabilities

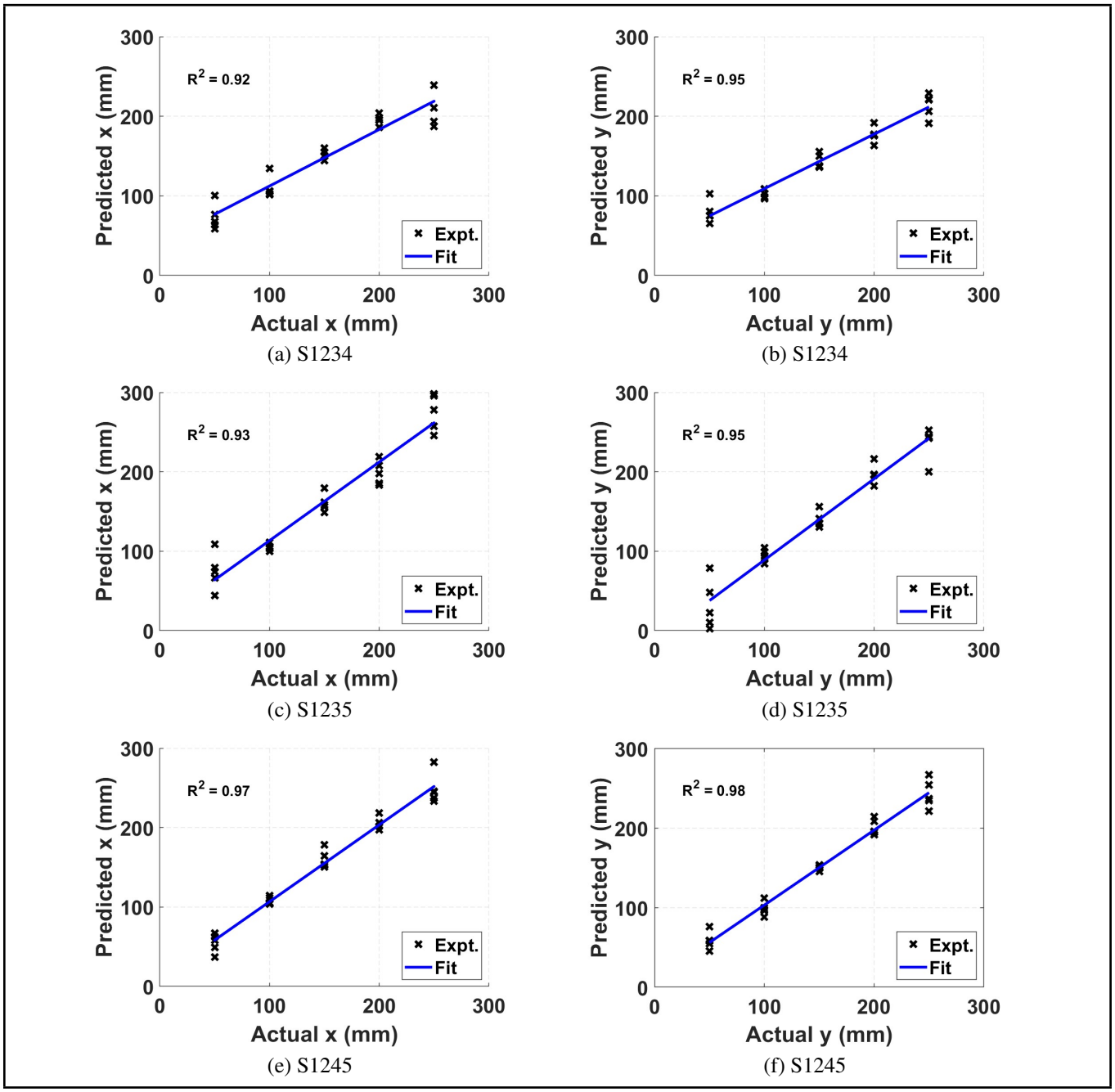

Figure 7. Regression analysis for impact coordinates performed under different sensor configurations using SA-GA framework.

exceeding 90% with low relative error of 5% and uncertainties below ± 5 mm for optimal sensor arrangements, even for impacts outside the region confined by piezoelectric sensor networks.

- The combined SA-GA approach outperformed standalone optimization methods, reducing impact coordinates uncertainty by at least 50% compared to individual algorithms.
- Sensor placement critically influenced the performance of the proposed framework, with optimal asymmetric triangular configurations achieving about 0.97 correlation coefficients between actual and predicted values.
- Full-field velocity mapping revealed the combined SA-GA produced the most spatially consistent velocity fields.

The combined SA-GA framework demonstrated clear advantages over standalone SA and GA in terms of accuracy and robustness. While the proposed framework has been successfully validated for isotropic aluminum plates, its extension to anisotropic and composite materials presents a valuable direction for future research. In such materials, directional dependence of wave velocity and more complex dispersion relations would require the framework to simultaneously solve for an anisotropic velocity field or incorporate a directional velocity model. Future work will explore adapting the SA-GA optimization to characterize these added complexities, with potential applications to layered composites, fiber-reinforced polymers, and additively manufactured (3D-printed) structures, where baseline-free monitoring is equally critical but more challenging due to inherent material heterogeneity and anisotropy. Furthermore, while this study evaluated pre-defined sensor geometries, determining a globally optimal sensor network for a structure is a critical challenge. Fu-

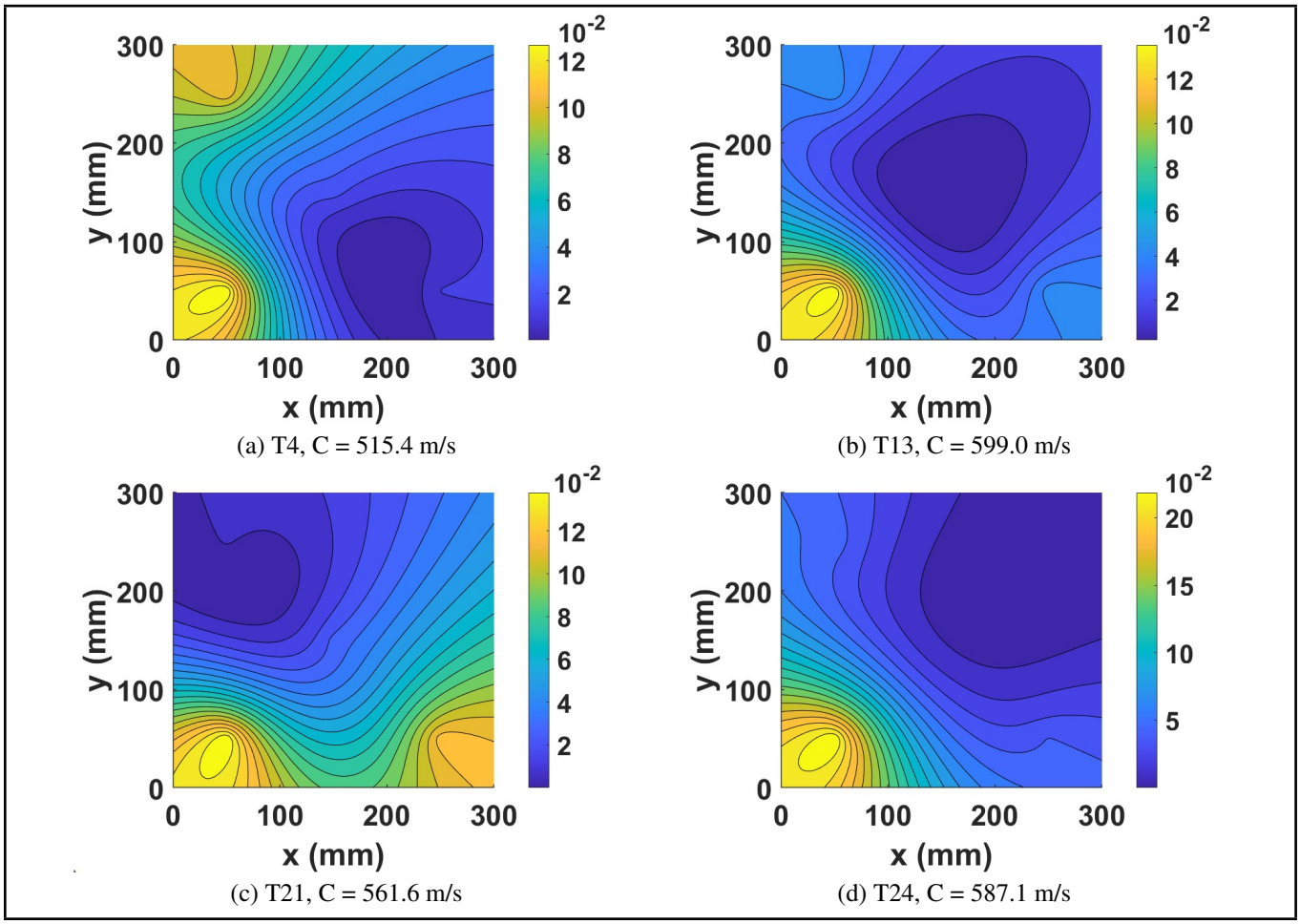

Figure 8. Surface diagrams of objective function at the mean group velocity using the SA-GA framework under optimal sensor arrangement.

ture work will investigate optimal sensor placement methods to be integrated with the proposed the proposed SA-GA framework to maximize localization accuracy for specific structural geometries and expected impact regions.

FUNDING

This work was supported by the Deanship of Scientific Research, Vice Presidency for Graduate Studies and Scientific Research, King Faisal University, Saudi Arabia, [Grant No. KFU252501].

REFERENCES

[1] Renson, L., Kerschen, G., and Cochelin, B. Numerical computation of nonlinear normal modes in mechanical engineering, *Journal of Sound and Vibration*, **364**, 177–206, (2016). https://doi.org/10.1016/j.jsv.2015.09.033

[2] Gagani, A. I., Krauklis, A. E., Sæter, E., Vedvik, N. P., and Echtermeyer, A. T. A novel method for testing and determining ILSS for marine and offshore composites, *Composite Structures*, **220**, 431–440, (2019). https://doi.org/10.1016/j.compstruct.2019.04.040

[3] Liang, H., Zou, J., Zuo, K., and Khan, M. J. An improved genetic algorithm optimization fuzzy controller applied to the wellhead back pressure control system, *Mechanical Systems and Signal Processing*, **142**, 106708, (2020). https://doi.org/10.1016/j.ymssp.2020.106708

[4] Moll, J., Maetz, T., Maelzer, M., Krozer, V., Mischke, K., Krause, S., Bagemiel, O., Nuber, A., Kremling, S., Kurin, T., Lurz, F., Weigel, R., and Issakov, V. Radar-based monitoring of glass fiber reinforced composites during fatigue testing, *Structural Control and Health Monitoring*, **28** (10), e2812, (2021). https://doi.org/10.1002/stc.2812

[5] Altammar, H. and Selimefendigil, F. Experimental characterization and probabilistic group velocity mapping of nondestructive impacts in plate structures using simulated annealing algorithm, *Structures*, **82**, 110558, (2025). https://doi.org/10.1016/j.istruc.2025.110558

[6] Duan, C., Makis, V., and Deng, C. Optimal Bayesian early fault detection for CNC equipment using hidden semi-Markov process, *Mechanical Systems and Signal Processing*, **122**, 290–306, (2019). https://doi.org/10.1016/j.ymssp.2018.11.040

[7] Spathelf, C. A. and Vogel, T. Fatigue performance of orthogonally reinforced concrete slabs: Experimental investigation, *Engineering Structures*, **168**, 69–81, (2018). https://doi.org/10.1016/j.engstruct.2018.04.058

[8] Lugo, L. J. P., Segura, C., and Miranda, G. Future trends in the design of memetic algorithms: The case of the linear ordering problem, *Neural Computing and Applications*, **37** (18), 12471–12485, (2025). https://doi.org/10.1007/s00521-025-11171-z

[9] Cotta, C. Harnessing memetic algorithms: A practical guide, *TOP*, **33** (2), 327–356, (2025). https://doi.org/10.1007/s11750-024-00694-8

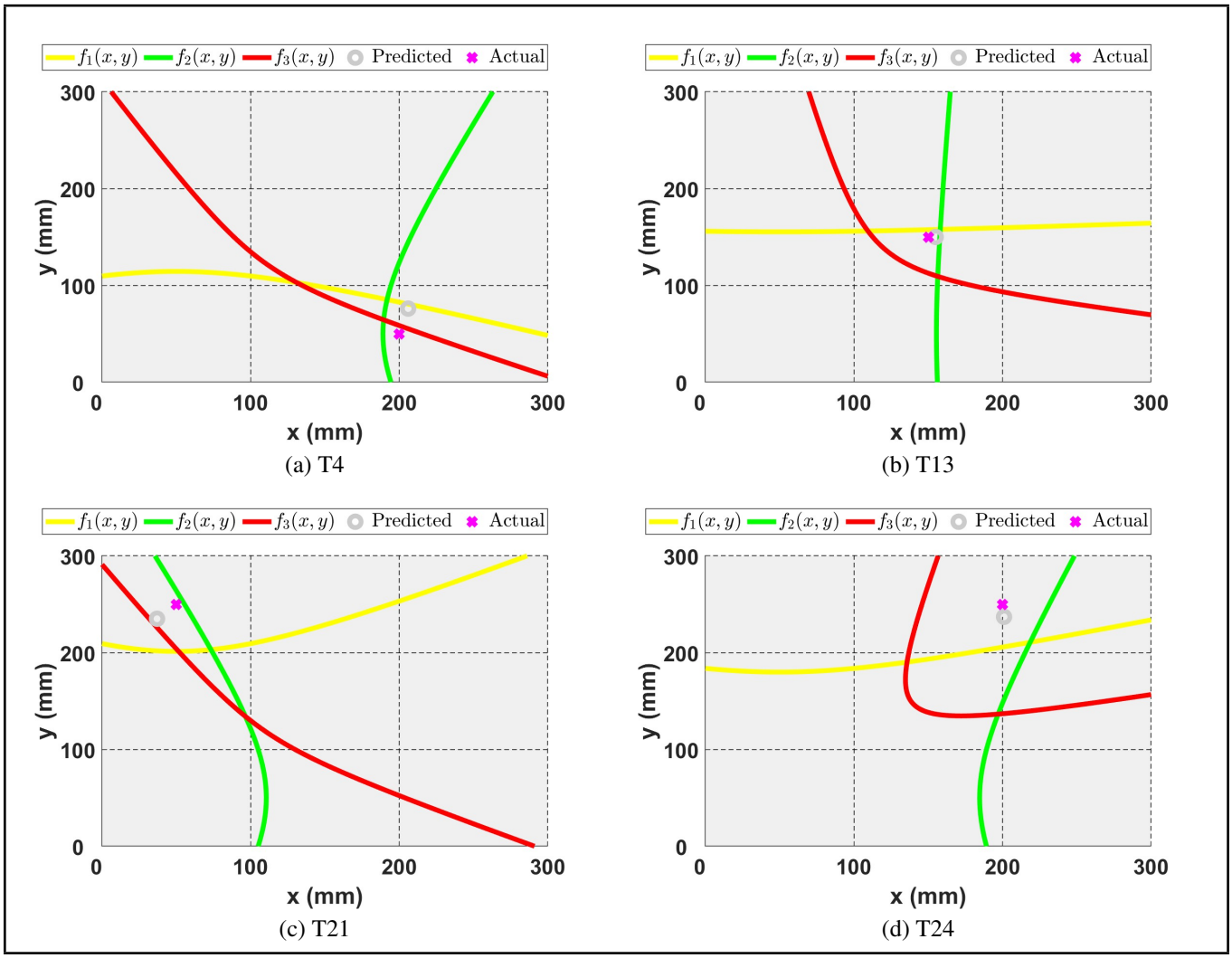

Figure 9. Comparison of SA-GA algorithm and deterministic solutions obtained using group velocity of A0 mode at 11.1 kHz under optimal sensor arrangement.

[10] Neri, F. and Cotta, C. Memetic algorithms and memetic computing optimization: A literature review, *Swarm and Evolutionary Computation*, **2**, 1–14, (2012). https://doi.org/10.1016/j.swevo.2011.11.003

[11] Rahman, I. and Mohamad-Saleh, J. Hybrid bio-inspired computational intelligence techniques for solving power system optimization problems: A comprehensive survey, *Applied Soft Computing*, **69**, 72–130, (2018). https://doi.org/10.1016/j.asoc.2018.04.051

[12] Talbi, E.-G. *Metaheuristics: From Design to Implementation*, Wiley, (2009). https://doi.org/10.1002/9780470496916

[13] Sörensen, K. Metaheuristics—the metaphor exposed, *International Transactions in Operational Research*, **22** (1), 3–18, (2015). https://doi.org/10.1111/itor.12001

[14] Mei, J., Wu, L., Chen, E., Xiao, W., Zhong, L., Guo, J., and Li, W. A novel structural damage detection method using a hybrid IDE–BP model, *Knowledge-Based Systems*, **273**, 110606, (2023). https://doi.org/10.1016/j.knosys.2023.110606

[15] Wang, J., Geng, L., Ding, L., Zhu, H., and Yurchenko, D. The state-of-the-art review on energy harvesting from flow-induced vibrations, *Applied Energy*, **267**, 114902, (2020). https://doi.org/10.1016/j.apenergy.2020.114902

[16] Zhang, T., Bubeck, R. A., Joffre, T. A., Bremmer, G. A., McNamara, L. P., Heydenburg, A. M., and Li, B. Promoting materials science and engineering education through 3d printing technology, *Proceedings of ASEE Annual Conference and Exposition*, 2020-June, (2020). https://doi.org/10.18260/1-2–35106

[17] Li, H. T., Dong, B. J., Cao, F., Xu, P., and Qin, W. Y. Improving the performance of wind energy galloping harvesting with magnetic coupling, *Epl*, **134** (3), (2021). https://doi.org/10.1209/0295-5075/134/30002

[18] Srinath, N., Yilmazlar, I. O., Kurz, M. E., and Taaffe, K. Hybrid multi-objective evolutionary meta-heuristics for a parallel machine scheduling problem with setup times and preferences, *Computers & Industrial Engineering*, **185**, 109675, (2023). https://doi.org/10.1016/j.cie.2023.109675

[19] Sonbul, O. S. and Rashid, M. Algorithms and techniques for the structural health monitoring of bridges: Systematic literature review, *Sensors*, **23** (9), 1–29, (2023). https://doi.org/10.3390/s23094230

[20] Mustapha, S., Ye, L., Dong, X., and Alamdari, M. M. Evaluation of barely visible indentation damage (BVID) in CF/EP sandwich composites using guided wave signals, *Mechanical Systems and Signal Processing*, (2016). https://doi.org/10.1016/j.ymssp.2016.01.023

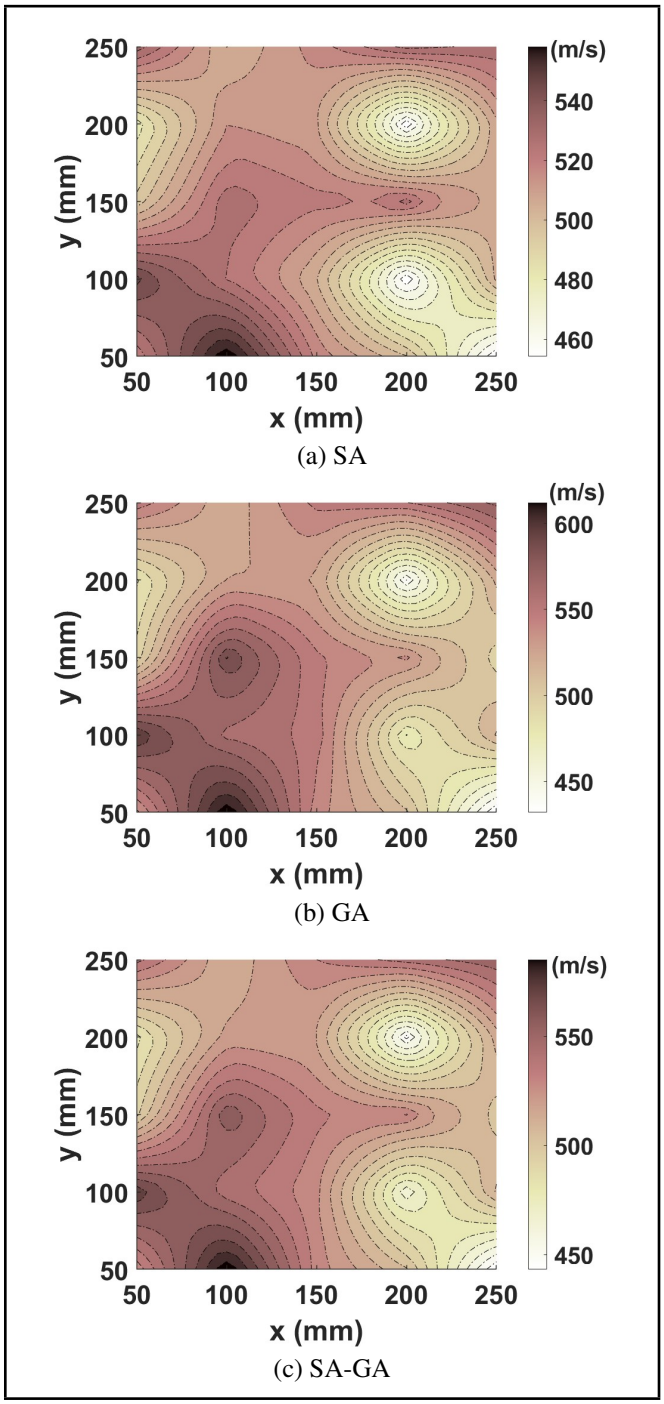

Figure 10. Comparison of full-field A0 mode group velocity mapping results from (a) SA, (b) GA, and (c) the combined SA-GA framework. It is reconstructed via bilinear interpolation from group velocities estimated at 25 grid points, each tested under three sensor configurations (75 total impacts). Velocities are in m/s.

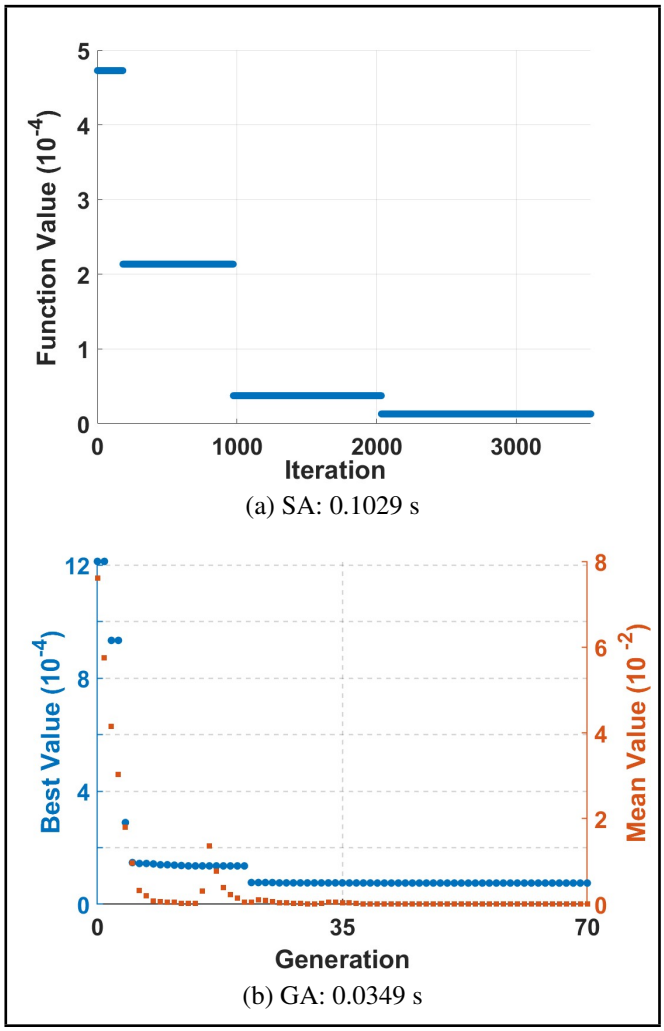

Figure 11. Solution convergence of a single run for impact test point (T4) under square sensor arrangement.

https://doi.org/10.1115/1.4050521

[23] Sohn, J. W., Ruth, J. S., Yuk, D. G., and Choi, S. B. Application of shape memory alloy actuators to vibration and motion control of structural systems: A review, *Applied Sciences*, **13** (2), (2023). https://doi.org/10.3390/app13020995

[24] Houdek, V., Smolík, L., and Kubín, Z. Impact point localization in three-dimensional structures using wavelet transform, *Mechanical Systems and Signal Processing*, **177**, 109091, (2022). https://doi.org/10.1016/j.ymssp.2022.109365

[25] Marinho, N. R., Loendersloot, R., Wiegman, J. W., Grooteman, F., and Tinga, T. Evaluating sensor performance for impact identification in composites: a comprehensive comparison of FBGs with PZTs, *Structural Health Monitoring*, (2025). https://doi.org/10.1177/14759217241304644

[26] Ma, G., Huang, Z., Wang, M., and Ji, Z. Performance analysis and sensor-target geometry optimization for toa and tdoa-based hybrid source localization method, *Applied Sciences*, **12** (7), 3543, (2022). https://doi.org/10.3390/app122412977

[27] Ochôa, P., Infante, V., Silva, J. M., and Groves, R. M. Detection of multiple low-energy impact damage in composite plates using lamb wave techniques,

[21] Dziendzikowski, M., Kurnyta, A., Dragan, K., Klysz, S., and Leski, A. In situ Barely Visible Impact Damage detection and localization for composite structures using surface mounted and embedded PZT transducers: A comparative study, *Mechanical Systems and Signal Processing*, **78**, 1–16, (2016). https://doi.org/10.1016/j.ymssp.2015.09.021

[22] Altammar, H. and Salowitz, N. Ultrasonic structural health monitoring approach to predict delamination in a laminated beam using d15 piezoelectric sensors, *Journal of Nondestructive Evaluation, Diagnostics and Prognostics of Engineering Systems*, **4**, 1–9, (2021).

Composites Part B: Engineering, **80**, 291–298, (2015). https://doi.org/10.1016/j.compositesb.2015.06.010

[28] Zhou, W., Pan, Zb., Wang, J., et al. Review on acoustic emission source location, damage recognition and lifetime prediction of fiber-reinforced composites, *Journal of Materials Science*, **58** (2), 583–607, (2023). https://doi.org/10.1007/s10853-022-08063-1

[29] Diamanti, K., Hodgkinson, J. M., and Soutis, C. Detection of low-velocity impact damage in composite plates using lamb waves, *Structural Health Monitoring*, **3** (1), 33–41, (2004). https://doi.org/10.1177/1475921704041869

[30] Altammar, H. and Khan, M. F. Evaluation of welded lap joints using ultrasonic guided waves, *Sensors*, **24**, 1384, (2024). https://doi.org/10.3390/s24051384

[31] Chandrashekhar, M. and Ganguli, R., Damage assessment of structures with uncertainty by using mode-shape curvatures and fuzzy logic, *Journal of Sound and Vibration*, **326**, 939–957, (2009). https://doi.org/10.1016/j.jsv.2009.05.030

[32] Beck, J. and Katefygiotis, L., Updating models and their uncertainties. I: Bayesian statistical framework, *Journal of Engineering Mechanics*, **124** (4), (1998). https://doi.org/10.1061/(ASCE)0733-9399(1998)124:4(455)

[33] Altammar, H. A probabilistic model-based framework for damage detection in beam-like structures considering temperature effects, *International Journal of Acoustics and Vibration*, **29** (4), 415–430, (2024). https://doi.org/10.20855/ijav.2024.29.42066

[34] Sun, L., Wei, J., Peng, C., Hao, W., Teng, F., Fan, L., Zhang, L., Sui, Q., and Jiang, M. Ultrasonic guided wave-based probabilistic diagnostic imaging method with single-path-scattering sparse reconstruction for multi-damage detection in composite structures, *Mechanical Systems and Signal Processing*, **223**, 111858, (2025). https://doi.org/10.1016/j.ymssp.2024.111858

[35] Hughes, A. J., Barthorpe, R. J., Dervilis, N., Farrar, C. R., and Worden, K. A probabilistic risk-based decision framework for structural health monitoring, *Mechanical Systems and Signal Processing*, **150**, 107339, (2021). https://doi.org/10.1016/j.ymssp.2020.107339

[36] Zhang, K., Li, H., Duan, Z., and Law, S. A probabilistic damage identification approach for structures with uncertainties under unknown input, *Mechanical Systems and Signal Processing*, **25**, 1126–1145, (2011). https://doi.org/10.1016/j.ymssp.2010.10.017

[37] Gad, A. G. Particle swarm optimization algorithm and its applications: A systematic review, *Archives of Computational Methods in Engineering*, **29** (6), 4757–4792, (2022). https://doi.org/10.1007/s11831-021-09694-4

[38] Kirkpatrick, S., Gelatt, C. D., and Vecchi, M. P. Optimization by simulated annealing, *Science*, **220** (4598), 671–680, (1983). https://doi.org/10.1126/science.220.4598.671

[39] Hashemi, R. and Kargarnovin, M. H. Vibration base identification of impact force using genetic algorithm, *International Journal of Mechanical Systems Science and Engineering*, **1** (4), 204–210, (2007).

[40] Hassan, F., Mahmood, A. W. B., Yahya, N., Saboor, A., Abbas, M. Z., Khan, Z., and Rimsan, M. State-of-the-art review on the acoustic emission source localization techniques, *IEEE Access*, **9**, 101246–101266, (2021). https://doi.org/10.1109/ACCESS.2021.3096930

[41] Bhandari, B., Maung, P. T. and Prusty, G. B., Novel response surface technique for composite structure localization using variable acoustic emission velocity, *Sensors*, **24** (1), 134, (2024). https://doi.org/10.3390/s24113450

[42] Hassani, S. and Dackermann, U. A systematic review of optimization algorithms for structural health monitoring and optimal sensor placement, *Sensors*, **23** (1), 112, (2023). https://doi.org/10.3390/s23063293

[43] Ostachowicz, W., Soman, R., and Malinowski, P. Optimization of sensor placement for structural health monitoring: A review, *Structural Health Monitoring*, **18** (3), 963–989, (2019). https://doi.org/10.1177/1475921719825601

[44] Bhuyan, M. D. H., Döhler, M., Lecieux, Y., Mevel, L., and Schoefs, F. Statistical damage localization with stochastic load vectors using multiple mode sets, *Structural Health Monitoring*, **16** (5), 518–535, (2017). https://doi.org/10.1177/1475921717714447

[45] Altammar, H. and Kaul, S., Adaptive probabilistic optimization approach for vibration-based structural health monitoring, *Signals*, **2** (3), 475–489, (2021). https://doi.org/10.3390/signals2030029

[46] Avci, O., Abdeljaber, O., Kiranyaz, S., Hussein, M., Gabbouj, M., and Inman, D. J. A review of vibration-based damage detection in civil structures: From traditional methods to Machine Learning and Deep Learning applications, *Mechanical Systems and Signal Processing*, **147**, 107077, (2021). https://doi.org/10.1016/j.ymssp.2020.107077

[47] Yoon, J., Lee, J., Kim, G., Ryu, S., and Park, J. Deep neural network-based structural health monitoring technique for real-time crack detection and localization using strain gauge sensors, *Scientific Reports*, **12** (1), 1–11, (2022). https://doi.org/10.1038/s41598-022-24269-4

[48] Malekloo, A., Ozer, E., AlHamaydeh, M., and Girolami, M. Machine learning and structural health monitoring overview with emerging technology and high-dimensional data source highlights, *Structural Health Monitoring*, **21** (4), 1906–1955, (2022). https://doi.org/10.1177/14759217211036880

[49] IEEE standard on piezoelectricity, ANSI/IEEE Std 176-1987, (1988). https://doi.org/10.1109/IEEESTD.1988.79638

[50] Li, X., Deng, Z. D., Rauchenstein, L. T., and Carlson, T. J. Contributed Review: Source-localization algorithms and applications using time of arrival and time difference of arrival measurements, *Review of Scientific Instruments*, **87** (4), 041502, (2016). https://doi.org/10.1063/1.4947001

[51] Savitzky, A. and Golay, M. J. E. Smoothing and differentiation of data by simplified least squares procedures, *Analytical Chemistry*, **36** (8), 1627–1639, (1964). https://doi.org/10.1021/ac60214a047